Supplemental Material

Supporting Information for ”Clarifying the relation between AMOC and thermal wind: application to the centennial variability in a coupled climate model”

Robin Waldman*

Centre National de Recherches Météorologiques, Toulouse, France

Joël Hirschi

National Oceanographic Centre, Southampton, United Kingdom

Aurore Voldoire

Centre National de Recherches Météorologiques, Toulouse, France

Christophe Cassou, Rym Msadek

CECI, Université de Toulouse, CNRS, CERFACS, Toulouse, France

**Corresponding author address:* Robin Waldman, Centre National de Recherches Météorologiques, Météo France - CNRS, 42 avenue Gaspard Coriolis, 31057 Toulouse Cédex 1, France.

E-mail: robin.waldman@meteo.fr

ABSTRACT

Contents of this file:

1. Text SI1 ”Eulerian versus residual mean overturning stream function” and Figure SI1
2. Text SI2 ”Depth versus density coordinate AMOC”
3. Text SI3 ”How the density anomaly profile controls the maximum overturning depth and the thermal wind transport” and Figures SI2 and SI3
4. Text SI4 ”Geostrophic AMOC computation with variable bathymetry”
5. Text SI5 ”Alternative formulations of the external mode transport”
6. Text SI6 ”Sensitivity tests” and Figures SI4, SI5 and SI6

SI1: Eulerian versus residual mean overturning stream function

The residual mean mass overturning stream function (Ψ_r, in kg/s) is the diagnostic variable recommended by the Ocean Model Intercomparison Project (OMIP) endorsed in the Coupled Model Intercomparison Project Phase 6 (CMIP6) exercise (Griffies et al. 2016). It includes, in addition to the Eulerian mean mass transport in the meridional plane, the eddy-induced mass transport from parametrized subgrid-scale processes, namely the Gent and McWilliams (1990) mesoscale parametrization and the Fox-Kemper et al. (2008) submesoscale parametrization in the CNRM-CM6 climate model (Voldoire et al. 2019). Those mass transports quantify the contribution of eddy fluxes to tracer advection and are as such associated with no Eulerian mean volume transport. They are hardly measurable and in particular they are not included in the long-term RAPID section of the AMOC at $26.5°N$. They are not directly related to the Eulerian mean Ekman and geostrophic transports, making any physical decomposition of AMOC more challenging.

As a consequence, we have used the Eulerian mean overturning stream function, which only includes the Eulerian mean volume transport resolved by CNRM-CM6 model and can be computed from the model's meridional velocities. Hence it is comparable to RAPID measurements and it formally relates to the thermal wind relation in the geostrophic approximation, which is a requirement of our AMOC physical decomposition. We evaluate here the difference between both AMOC definitions. Overall, the Eulerian mean (Ψ, Fig.1a) overturning stream function is weaker than its residual mean counterpart (Ψ_r/ρ_0 with $\rho_0 = 1025 kg/m^3$, Fig.SI1a) by a few Sverdrups over the AMOC cell of the Atlantic ocean (Fig.1). This is confirmed by the mean AMOC (Fig.1b) which is increased by 11 to 25% south of $60°N$ when including the eddy-induced transport. At the latitude of the RAPID array, it is increased by 14%, whereas at the latitudes of the OSNAP section ($52-60°N$, Lozier et al. (2017)) it is increased by 18%. However, both AMOC definitions have an interannual correlation above 0.95 south of $60°N$, thus indicating that the AMOC variability is mostly not eddy-driven. We conclude that the mean AMOC significantly differs in CNRM-CM6 when computed as a residual mean transport, which biases model evaluation against observations, but that its interannual variability remains unchanged.

SI2: Depth versus density coordinate AMOC

In our study, we establish a simple diagnostic relation between the depth coordinate AMOC (hereafter $AMOC_z$) variability and density anomalies at zonal boundaries of the Atlantic Ocean. We show here that because of a zonally-varying interface depth, no such simple relation exists for the density coordinate AMOC (hereafter $AMOC_\sigma$). We first recall the main differences between both AMOC definitions. The overturning circulation of the Atlantic ocean has historically been quantified with $AMOC_z$ (e.g. the RAPID array). It is a Eulerian transport, and as such it is easily calculated from the zonal section of meridional velocities. It dominates the northward oceanic heat transport outside of subpolar latitudes (McCarthy et al. 2015). However, over the past two decades, $AMOC_\sigma$ has been extensively used for studies of the subpolar North Atlantic (e.g. OVIDE and OSNAP arrays, Mercier et al. (2015); Lozier et al. (2019)). It is a residual mean transport because it depends on zonal co-variations of meridional velocities and the interface depth between the upper and lower AMOC limbs, which is an isopycnal. Therefore, it is more challenging to calculate as it should be computed online at the model time step frequency in numerical simulations. However, it dominates the northward oceanic heat transport at all latitudes of the Atlantic Ocean and it relates naturally to water mass transformations in density space.

Let us illustrate the main dynamical difference between $AMOC_z$ and $AMOC_\sigma$ in the rectangular basin case. The AMOC transport is:

$$AMOC = \int_{x_W}^{x_E} \int_{d}^{0} v \, dz dx$$

with d either the constant depth z_m of maximum overturning for $AMOC_z$ or the zonally-variable isopycnal depth d_m (corresponding to the density σ_m of maximum overturning) for $AMOC_\sigma$. Its geostrophic component can be expressed as an integral zonal pressure force exerted by the volume of fluid at its boundaries:

$$\begin{aligned} AMOC_g &= \int_{x_W}^{x_E} \int_d^0 v_g(x,y,z,t)dzdx \\ &= \frac{1}{\rho_0 f} \int_{x_W}^{x_E} \int_d^0 \frac{\partial P}{\partial x} dzdx \end{aligned}$$

with x_W and x_E the western and eastern boundaries, v_g the meridional geostrophic velocity and P the pressure. Leibniz integration formula allows to write this pressure gradient as an interior plus an interfacial pressure force:

$$\begin{aligned} AMOC_g &= \frac{1}{\rho_0 f} \int_{x_W}^{x_E} \Big(\frac{\partial}{\partial x} \int_d^0 Pdz + P(d) \frac{\partial d}{\partial x} \Big) dx \\ &= \frac{1}{\rho_0 f} \left(\int_{d(x_E)}^0 P(x_E, z)dz - \int_{d(x_W)}^0 P(x_W, z)dz + \int_{x_W}^{x_E} P(d) \frac{\partial d}{\partial x} dx \right) \\ &= \frac{1}{\rho_0 f} \left(\Delta \Big(\int_d^0 Pdz \Big) + \Delta x \overline{P(d) \frac{\partial d}{\partial x}} \right) \end{aligned}$$

with $\Delta x = x_E - x_W$ the basin zonal width, $\Delta(A(x)) = A(x_E) - A(x_W)$ for any function $A(x)$ and the overline denoting a zonal average. The first term represents the pressure force exerted by the volume of fluid onto the solid Earth at the lateral boundaries, and will be referred to as the "lateral pressure force". In the general case of a sloping bottom, this term becomes a bottom form stress exerted onto topography above the depth z_m. The second term is the so-called "interfacial form stress", which represents the zonal pressure force exerted at the interface d onto the underlying fluid.

We now replace the lower depth d by the depth z_m of maximum meridional overturning in vertical coordinate and the depth $d_m = d(\sigma = \sigma_m)$ with σ_m the density of maximum meridional overturning in density coordinate, respectively. We obtain the respective expressions for the geostrophic component of the $AMOC$ in depth and density coordinates:

$$
\begin{aligned}
AMOC_{zg} &= \frac{1}{\rho_0 f}\int_{z_m}^{0}\Delta P dz \\
AMOC_{\sigma g} &= \frac{1}{\rho_0 f}\left(\Delta\Big(\int_{d_m}^{0} P dz\Big) + \Delta x \overline{P(d_m)\frac{\partial d_m}{\partial x}}\right)
\end{aligned}
$$

It appears clearly that the main difference between both formulations of the $AMOC$ is that the in-ferfacial form stress is a source of net meridional transport for the $AMOC_\sigma$ and not for the $AMOC_z$. Indeed, because of a slanted lower boundary d_m, a net zonal pressure force can be exerted onto the lower fluid. As a consequence of the geostrophic balance, this interfacial form stress induces a net meridional geostrophic flow above the depth d_m. This latter term depends on the zonal profile of pressure at the interface, which is a function of the full zonal density section and dynamic sea level profile, and of the zonal profile of the isopycnal interface depth. As a consequence, no simple relation can be derived between $AMOC_\sigma$ and hydrographic properties at zonal boundaries. This is why $AMOC_\sigma$ has been discarded from our dynamical analysis, although we acknowledge its relevance for the study of meridional heat transports and water mass transformations (e.g. Mercier et al. (2015); Lozier et al. (2019)).

SI3: How the density anomaly profile controls the maximum overturning depth and the thermal wind transport

Determination of the maximum overturning depth

In section 2e, we have established the depth dependency of the thermal wind transport $TW(z)$ and concluded that a given density anomaly induces most $AMOC_{g-sh}$ transport if it occurs at the depth z_m of maximum overturning. However, our diagnostic relation for a given depth z_m does not predict what controls that depth. If we only consider the vertically-compensated geostrophic $AMOC_{g-sh}$ transport, that depth is a function of the full vertical profile of density times either depth, or height above bottom. Indeed, the derivative of $AMOC_{g-sh}$ as a function of z_m is:

$$
\begin{aligned}
\frac{\partial AMOC_{g-sh}}{\partial z_m} &= \frac{g}{\rho_0 f}\left(\int_{-h}^{z_m}(1+\frac{z'}{h})\Delta\rho dz' + z_m(1+\frac{z_m}{h})\Delta\rho - z_m\Delta\rho + \int_{z_m}^{0}\frac{z'}{h}\Delta\rho dz' - z_m\frac{z_m}{h}\Delta\rho\right)\\
&= \frac{g}{\rho_0 f}\left(\int_{-h}^{z_m}(1+\frac{z'}{h})\Delta\rho dz' + \int_{z_m}^{0}\frac{z'}{h}\Delta\rho dz'\right)
\end{aligned}
$$

where we have applied the formulas for the derivatives of a product and of an integral. The first term is the transport increase due to the increasing thickness of the upper limb, which is fully impacted by density anomalies occurring below z_m. The second term is the transport reduction due to the increasing barotropic compensation of baroclinic transports driven by densities above z_m. Near surface, the first term is larger so that the transport increases with depth. Near the bottom, the second term is larger so that the transport decreases with depth. In between, the depth of maximum overturning is reached when both terms are equal and opposite in sign, meaning that the transport reduction due to the upper limb densities exactly compensates the transport increase due to lower limb densities. Mathematically, it is :

$$
\begin{aligned}
\frac{\partial AMOC_{g-sh}}{\partial z_m} &= 0\\
\Longrightarrow \int_{-h}^{z_m}(1+\frac{z'}{h})\Delta\rho dz' &= \int_{z_m}^{0}\frac{-z'}{h}\Delta\rho dz'
\end{aligned}
$$

This relation shows that the depth z_m depends crucially on the density anomaly profile. Qualitatively, the larger the near-surface density anomalies, the shallower the maximum overturning and the shallower the density anomalies that induce most upper limb transport. In the particular case of a constant density anomaly at all depths, we obtain :

$$
\begin{aligned}
\frac{\partial AMOC_{g-sh}}{\partial z_m} &= 0 \\
\Longrightarrow \left[z' + \frac{z'^2}{2h}\right]_{-h}^{z_m} + \left[\frac{z'^2}{2h}\right]_{z_m}^{0} &= 0 \\
\Longrightarrow z_m + h - \frac{h}{2} &= 0 \\
\Longrightarrow z_m &= -\frac{h}{2}
\end{aligned}
$$

that is, a maximum overturning at mid-depth $\frac{h}{2}$, and therefore a maximum thermal wind transport $TW(z)$ induced by density anomalies at that depth.

We illustrate the dependency of the maximum overturning depth on the density anomaly profile with Fig. SI2. Two vertically-symmetric profiles are shown with density anomalies located either near the surface (left) or near the bottom (right). In the former case (left), the near-surface negative density anomaly induces a positive (Northern Hemisphere) vertical shear of geostrophic velocities. By mass conservation the vertical mean sheared velocity must cancel out, hence positive velocities from the surface to near the base of the density anomaly, and negative velocities below. As a consequence, the associated stream function increases from surface to the depth where sheared velocities go to zero, and then decreases down to the bottom. The resulting depth z_m of maximum overturning is close to the surface, near the basis of the density anomalies. Symmetrically, in the latter case (right), near-bottom density anomalies cause a vertical shear of geostrophic velocities and as a result of mass conservation, positive velocities from surface to near the top of the density anomalies, and then negative anomalies below. The associated overturning stream function reaches a maximum at a depth z_m near the bottom, next to the top of density anomalies.

Determination of the maximum thermal wind transport

We have shown that the density anomaly profile plays a key role in determining the depth of maximum overturning. Here we illustrate how this depth of maximum overturning, together with the density anomaly profile, controls the thermal wind transport TW. We recall that this thermal wind transport, in Sv/m, quantifies the contribution of density anomalies at a given depth to the sheared geostrophic transport above z_m, so that its vertical integral is the value of the overturning stream function at z_m. Fig. SI2 shows that the thermal wind transport is only positive at the depth where density anomalies occur, and that for a given density anomaly, the closer to the maximum overturning depth z_m, the larger TW. As a consequence, TW is maximum near the basis of the surface-intensified density anomalies (left), and near the top of the bottom-intensified density anomalies (right). For a given density anomaly, TW decreases linearly towards the surface and bottom, to cancel out at both boundaries.

Fig. SI3 illustrates how for a given z_m, the magnitude of the thermal wind transport is proportional to that of density anomalies. In both examples, density anomalies are located at mid-depth, so that geostrophic velocities change sign at that depth and the resulting depth of maximum overturning is $z_m = -h/2$. The only difference is the doubling of the magnitude of density anomalies in the second case (right) compared to the first one (left). As a result, sheared velocities and their overturning stream function are also doubled, as well as TW(z) at the depths where density anomalies occur. The maximum overturning, which is by definition the vertical integral of the thermal wind transport, is therefore also doubled in the latter case.

SI4: Geostrophic AMOC computation with variable bathymetry

Let us first consider a zonal section with strictly increasing topography on both sides of the deepest bathymetry $-h_b$. In this case, the baroclinic geostrophic transport of AMOC is insensitive to topographic details. The only requirement is to consider at each depth the easternmost and westernmost densities for the computation of the baroclinic geostrophic AMOC transport. Indeed, we have:

$$
\begin{aligned}
AMOC_{BCg} &= -\frac{g}{\rho_0 f}\int_{z_m}^{0}\int_{x_W(z)}^{x_E(z)}\int_{-h(x)}^{z}\frac{\partial\rho}{\partial x}(z')dz'dxdz \\
&= -\frac{g}{\rho_0 f}\int_{x_W(0)}^{x_E(0)}\int_{max(-h,z_m)}^{0}\int_{-h(x)}^{z}\frac{\partial\rho}{\partial x}(z')dz'dzdx \\
&= -\frac{g}{\rho_0 f}\int_{x_W(0)}^{x_E(0)}\int_{max(-h,z_m)}^{0}\left(\int_{-h(x)}^{max(-h,z_m)}\frac{\partial\rho}{\partial x}(z')dz'+\int_{max(-h,z_m)}^{z}\frac{\partial\rho}{\partial x}(z')dz'\right)dzdx \\
&= +\frac{g}{\rho_0 f}\int_{x_W(0)}^{x_E(0)}\left(\int_{-h(x)}^{max(-h,z_m)}max(-h,z_m)\frac{\partial\rho}{\partial x}dz'+\int_{max(-h,z_m)}^{0}z'\frac{\partial\rho}{\partial x}dz'\right)dx \\
&= +\frac{g}{\rho_0 f}\left(\int_{x_W(z_m)}^{x_E(z_m)}\int_{-h(x)}^{z_m}z_m\frac{\partial\rho}{\partial x}dz'dx+\int_{x_W(0)}^{x_E(0)}\int_{max(-h,z_m)}^{0}z'\frac{\partial\rho}{\partial x}dz'dx\right)
\end{aligned}
$$

where we have used the double integration rule. In the last step, we have noted that the first integral vanishes when $h < -z_m$, so that integrals between $x_W(0)$ and $x_W(z_m)$ and between $x_E(0)$ and $x_E(z_m)$ vanish and $max(-h,z_m) = z_m$ between $x_W(z_m)$ and $x_E(z_m)$, since $h > -z_m$. Finally, reversing the order of integration and integrating zonally yields:

$$
\begin{aligned}
AMOC_{BCg} &= +\frac{g}{\rho_0 f}\left(\int_{-h_b}^{z_m}\int_{x_W(z)}^{x_E(z)}z_m\frac{\partial\rho}{\partial x}dxdz+\int_{z_m}^{0}\int_{x_W(z)}^{x_E(z)}z\frac{\partial\rho}{\partial x}dxdz\right) \\
&= +\frac{z_m g}{\rho_0 f}\int_{-h_b}^{z_m}\Big(\rho(x_E(z),z)-\rho(x_W(z),z)\Big)dz+\frac{g}{\rho_0 f}\int_{z_m}^{0}z\Big(\rho(x_E(z),z)-\rho(x_W(z),z)\Big)dz \\
&= +\frac{z_m g}{\rho_0 f}\int_{-h_b}^{z_m}\Delta\rho(z)dz+\frac{g}{\rho_0 f}\int_{z_m}^{0}z\Delta\rho(z)dz
\end{aligned}
$$

with $\Delta\rho(z) = \Big(\rho(x_E(z),z)-\rho(x_W(z),z)\Big)$. The reversal of vertical and zonal integrals is allowed by the assumption of a strictly monotonic batymetry on both sides of h_b, which is the mathematical translation of the neglect of ridges and islands. The above expression is identical to the rectangular basin case, but we evaluate the boundary density at the westernmost and easternmost location of each depth, and we integrate the thermal wind relation from the deepest bathymetry h_b.

The section-integrated meridional transport becomes:

$$
\begin{aligned}
\Psi(-h_b) &= AMOC_E + \int_{-h_b}^{0}\int_{x_W(z)}^{x_E(z)} \left(v_g(-h) - \frac{g}{\rho_0 f}\int_{-h(x)}^{z} \frac{\partial \rho}{\partial x}(z')dz' \right) dxdz \\
&= AMOC_E + \int_{x_W(0)}^{x_E(0)}\int_{-h(x)}^{0} \left(v_g(-h) - \frac{g}{\rho_0 f}\int_{-h(x)}^{z} \frac{\partial \rho}{\partial x}(z')dz' \right) dzdx \\
&= AMOC_E + \int_{x_W(0)}^{x_E(0)} \left(h(x)v_g(-h) - \frac{g}{\rho_0 f}\int_{-h(x)}^{0}\int_{z'}^{0} \frac{\partial \rho}{\partial x}(z')dzdz' \right) dx \\
&= AMOC_E + \Delta x(0)\overline{hv_g(-h)} + \frac{g}{\rho_0 f}\int_{x_W(0)}^{x_E(0)}\int_{-h(x)}^{0} z'\frac{\partial \rho}{\partial x}(z')dz'dx \\
&= AMOC_E + \Delta x(0)\left(\overline{h}\,\overline{v_g(-h)} + \overline{h' v_g(-h)'}\right) + \frac{g}{\rho_0 f}\int_{-h_b}^{0} z\Delta\rho(z)dz
\end{aligned}
$$

where $\Delta x(0) = x_E(0) - x_W(0)$ and the overline and prime denote a zonal mean and anomaly. We have simplified the double vertical integral and reversed zonal and vertical integral similarly as for $AMOC_{BCg}$. The term involving zonal anomalies is part of the so-called "external mode", which is the only explicit dependency to the reference vertical level chosen for the thermal wind integration. It can be viewed as a projection of the barotropic (gyre) transport onto the AMOC. We finally get:

$$
\begin{aligned}
\Psi(-h_b) &= 0 \\
\Longleftrightarrow \overline{v_g(-h)} &= -\frac{1}{\overline{h}\Delta x(0)}\left(AMOC_E + \Delta x(0)\overline{h' v_g(-h)'} + \frac{g}{\rho_0 f}\int_{-h_b}^{0} z\Delta\rho(z)dz \right)
\end{aligned}
$$

which yields the barotropic geostrophic transport of AMOC:

$$
\begin{aligned}
AMOC_{BTg} &= \int_{z_m}^{0}\int_{x_W(z)}^{x_E(z)} v_g(-h)dxdz \\
&= \int_{x_W(0)}^{x_E(0)}\int_{max(-h,z_m)}^{0} v_g(-h)dzdx \\
&= -\int_{x_W(0)}^{x_E(0)} v_g(-h)\,max(-h,z_m)dx \\
&= +\int_{x_W(0)}^{x_E(0)} v_g(-h)\,min(h,-z_m)dx \\
&= \Delta x(0)\overline{v_g(-h)\,min(h,-z_m)} \\
&= \Delta x(0)\Big(\overline{v_g(-h)}\,\overline{min(h,-z_m)}+\overline{min(h,-z_m)'\,v_g(-h)'}\Big) \\
&= \Delta x(0)\Big(-\overline{v_g(-h)}\overline{z_m}+\overline{min(h,-z_m)'\,v_g(-h)'}\Big)
\end{aligned}
$$

where $\overline{z_m} = -\overline{min(h,-z_m)}$ is the mean depth of the upper limb AMOC zonal section. Finally, expressing $\overline{v_g(-h)}$ as deduced from the no net meridional flow condition gives:

$$
AMOC_{BTg} = +\frac{\overline{z_m}}{\overline{h}}\left(AMOC_E+\frac{g}{\rho_0 f}\int_{-h_b}^{0} z\Delta\rho(z)dz\right)+\Delta x(0)\left(\frac{\overline{z_m}}{\overline{h}}\overline{h' v_g(-h)'}+\overline{min(h,-z_m)'\,v_g(-h)'}\right)
$$

Again, it resembles the rectangular basin case. Similarly to $AMOC_{BCg}$, the zonal and vertical thermal wind integrations are little modified. We have replaced the factor z_m/h by its zonal average $\overline{z_m}/\overline{h}$, which still represents the fraction of the total barotropic transport that is located in the upper AMOC limb. Most importantly, we have added the "external mode" which represents the zonal covariance of $v_g(-h)$ with bathymetry and the upper limb depth:

$$
AMOC_{g-EM} = \Delta x(0)\left(\frac{\overline{z_m}}{\overline{h}}\overline{h' v_g(-h)'}+\overline{min(h,-z_m)'\,v_g(-h)'}\right)
$$

It is generally not null because of the existence of boundary currents that lean on topographic obstacles, and hence non-null covariances between bottom velocity and either bathymetry or the upper limb depth. In section SI5, we show that the external mode can be equivalently expressed as an integral corrected bottom velocity (Baehr et al. 2004) or barotropic velocity (Hirschi and Marotzke 2007). Finally, we obtain an almost identical expression for the AMOC as in the rectangular basin case, with the addition of the ”external mode” (equation 19):

$$\begin{aligned} AMOC &= -(1+\frac{\overline{z_m}}{\overline{h}})\frac{\Delta x(0)}{\rho_0 f}\overline{\tau_x} + \frac{g}{\rho_0 f}\Big(\int_{-h_b}^{z_m}(z_m+\frac{\overline{z_m}}{\overline{h}}z)\Delta\rho(z)dz + \int_{z_m}^{0} z(1+\frac{\overline{z_m}}{\overline{h}})\Delta\rho(z)dz\Big) \\ &\quad + \Delta x(0)\left(\frac{\overline{z_m}}{\overline{h}}\overline{h' v_g(-h)'} + \overline{min(h,-z_m)' v_g(-h)'}\right) \end{aligned}$$

In the general case of a non-monotonic topography (e.g. in the presence of ridges and islands), the basin can be divided into a discrete number $n > 1$ of subbasins of strictly monotonic bathymetry. The above $AMOC_{BCg}$ formulation remains valid for each subbasin of index i, with its zonal boundaries being either closed by bathymetry or open above seamounts. The total $AMOC_{BCg}$ transport becomes:

$$\begin{aligned} AMOC_{BCg} &= \sum_{i=1}^{n}\left(\frac{z_m g}{\rho_0 f}\int_{-h_b}^{z_m}\Delta\rho_i(z)dz + \frac{g}{\rho_0 f}\int_{z_m}^{0} z\Delta\rho_i(z)dz\right) \\ &= \frac{z_m g}{\rho_0 f}\int_{-h_b}^{z_m}\Big(\sum_{z=-h(x_{Ei})}\rho(x_{Ei},z) - \sum_{z=-h(x_{Wi})}\rho(x_{Wi},z)\Big)dz \\ &\quad + \frac{g}{\rho_0 f}\int_{z_m}^{0} z\Big(\sum_{z=-h(x_{Ei})}\rho(x_{Ei},z) - \sum_{z=-h(x_{Wi})}\rho(x_{Wi},z)\Big)dz \end{aligned}$$

where we have noted that densities at open boundaries cancel out, so that only bottom densities (where $z=-h(x_{Ei})$ and $z=-h(x_{Wi})$) affect the $AMOC_{BCg}$ transport. With a similar development for the barotropic compensation of the net baroclinic flow, the $AMOC_{BTg}$ becomes:

$$\begin{aligned} AMOC_{BTg} &= \frac{\overline{z_m}}{\overline{h}}\left(AMOC_E + \frac{g}{\rho_0 f}\int_{-h_b}^{0} z\Big(\sum_{z=-h(x_{Ei})}\rho(x_{Ei},z) - \sum_{z=-h(x_{Wi})}\rho(x_{Wi},z)\Big)dz\right) \\ &\quad + AMOC_{g-EM} \end{aligned}$$

Finally, the AMOC reconstruction becomes:

$$
\begin{aligned}
AMOC &= -(1+\frac{\overline{z_m}}{\overline{h}})\frac{\Delta x(0)}{\rho_0 f}\overline{\tau_x} \\
&+\frac{g}{\rho_0 f}\Big(\int_{-h_b}^{z_m}(z_m+\frac{\overline{z_m}}{\overline{h}}z)\Big(\sum_{z=-h(x_{Ei})}\rho(x_{Ei},z)-\sum_{z=-h(x_{Wi})}\rho(x_{Wi},z)\Big)dz \\
&+\int_{z_m}^{0} z(1+\frac{\overline{z_m}}{\overline{h}})\Big(\sum_{z=-h(x_{Ei})}\rho(x_{Ei},z)-\sum_{z=-h(x_{Wi})}\rho(x_{Wi},z)\Big)dz\Big) \\
&+\Delta x(0)\left(\frac{\overline{z_m}}{\overline{h}}\overline{h' v_g(-h)'}+\overline{min(h,-z_m)' v_g(-h)'}\right)
\end{aligned}
$$

It is almost identical to the single basin case, except that instead of evaluating the westernmost and easternmost density at each depth, all western and eastern boundary densities contribute to the geostrophic shear AMOC transport, their number depending on depth and latitude. We evaluate both AMOC reconstructions in SI6 to show that the single boundary definition gives an accurate approximation of the $AMOC_{g-sh}$ transport in the CNRM-CM6 model.

SI5: Alternative formulations of the external mode transport

We demonstrate here that the external mode AMOC transport $AMOC_{g-EM}$ of equation 19 is identical to the overturning contribution originated from bottom velocities of Baehr et al. (2004) (their equations 11 and 12) and to the external mode resulting from barotropic velocities of Hirschi and Marotzke (2007) (their equations 1 and 16).

The overturning contribution at the depth z_m, $\Psi_b(z_m)$, originated by the bottom velocities, is defined by Baehr et al. (2004) as:

$$
\begin{aligned}
\Psi_b(z_m) &= -\int_{-h_b}^{z_m}\int_{x_W(z)}^{x_E(z)} v_{corr}(-h)dxdz \\
&= +\int_{z_m}^{0}\int_{x_W(z)}^{x_E(z)} v(-h)dxdz+\frac{\overline{z_m}}{\overline{h}}\int_{-h_b}^{0}\int_{x_W(z)}^{x_E(z)} v(-h)dxdz \\
&\simeq \int_{z_m}^{0}\int_{x_W(z)}^{x_E(z)} v_g(-h)dxdz+\frac{\overline{z_m}}{\overline{h}}\int_{-h_b}^{0}\int_{x_W(z)}^{x_E(z)} v_g(-h)dxdz
\end{aligned}
$$

where we have used the no net volumic flow condition in the first step, and we have assumed, as it is implicitly done by Baehr et al. (2004), that bottom velocities are geostrophic in order to reconstruct a geostrophic plus Ekman AMOC transport. The second term is the contribution of the section-averaged bottom geostrophic velocities to the AMOC, which is cancelled out by the no net volumic flow condition. Note that we have corrected an error of sign in equation 11 of Baehr et al. (2004), and an error in the upper bound of vertical integration in their equation 12. Reverting the order of integration and decomposing $v_g(-h)$, h and $min(z_m,h)$ into their zonal mean and anomaly, we obtain:

$$
\begin{aligned}
\Psi_b(z_m) &= \int_{x_W(0)}^{x_E(0)} \int_{max(z_m,-h)}^{0} v_g(-h)dxdz + \frac{\overline{z_m}}{\overline{h}} \int_{x_W(0)}^{x_E(0)} \int_{-h(x)}^{0} v_g(-h)dxdz \\
&= \int_{x_W(0)}^{x_E(0)} \int_{min(h,-z_m)}^{0} v_g(-h)dx + \frac{\overline{z_m}}{\overline{h}} \int_{x_W(0)}^{x_E(0)} h(x)v_g(-h)dx \\
&= \int_{x_W(0)}^{x_E(0)} min(h,-z_m)v_g(-h)dx - \frac{\overline{z_m}}{\overline{h}} \int_{x_W(0)}^{x_E(0)} h(x)v_g(-h)dx \\
&= \Delta x(0)\left(-\overline{z_m}\,\overline{v_g(-h)} + \overline{min(h,-z_m)'v_g(-h)'} + \frac{\overline{z_m}}{\overline{h}}\left(\overline{h}\,\overline{v_g(-h)} + \overline{h'v_g(-h)'}\right)\right) \\
&= \Delta x(0)\left(\overline{min(h,-z_m)'v_g(-h)'} + \frac{\overline{z_m}}{\overline{h}}\overline{h'v_g(-h)'}\right) \\
&= AMOC_{g-EM}
\end{aligned}
$$

defining $\overline{z_m} = -\overline{min(h,-z_m)}$ as in SI2. The equivalence of both formulations means that the external mode transport resulting from zonal covariances of $v_g(-h)$ with bathymetry or the upper limb depth is identical to the upper limb transport resulting from bottom velocities to which the section averaged value has been removed to ensure no net volumic flow.

The external mode transport Ψ_{ex} of Hirschi and Marotzke (2007) (their equation 16) results from barotropic velocities. Let us first reformulate the barotropic velocities v_{BT} of Hirschi and Marotzke (2007). Under their decomposition of equation 16 (equivalent to our equation 19), v_{BT} is not the vertical mean velocity (their equation 1), because the shear velocity v_{sh} is expressed with a zonally-integrated compensation (their equation 12) so that it ”contain[s] a barotropic contribution” (Hirschi and Marotzke (2007), paragraph after their equation 14). As a consequence:

$$\begin{aligned} v_{BT} &= <v> - <v_{sh}> \\ &= <v> - <v_{BCg}> + \frac{1}{\overline{h}\Delta x(0)} \int_{x_W}^{x_E} \int_{-h}^{0} v_{BCg} dz dx \end{aligned}$$

with $<>$ the vertical averaging operator, and $v_{BCg} = v_g - v_g(-h)$ the baroclinic geostrophic velocities deduced from the thermal wind relation (identical to $\tilde{v}$ of Hirschi and Marotzke (2007)). We note that by definition:

$$\begin{aligned} <v> &= <v_g(-h)> + <v_{BCg}> + <v_E> \\ &= v_g(-h) + <v_{BCg}> + \frac{V_E}{h} \end{aligned}$$

with V_E the vertically-integrated Ekman transport. Therefore:

$$v_{BT} = v_g(-h) + \frac{1}{\overline{h}\Delta x(0)} \int_{x_W}^{x_E} \int_{-h}^{0} v_{BCg} dz dx + \frac{V_E}{h}$$

Identically to our section SI4, the no net basin-scale flow constraint is:

$$\overline{v_g(-h)} = -\frac{1}{\overline{h}\Delta x(0)} \left(AMOC_E + \Delta x(0) \overline{h' v_g(-h)'} + \int_{x_W}^{x_E} \int_{-h}^{0} v_{BCg} dz dx \right)$$

Finally, the external mode AMOC transport of Hirschi and Marotzke (2007) is:

$$\begin{aligned} \Psi_{ex} &= \int_{x_W}^{x_E} \int_{z_m}^{0} v_{BT} dz dx \\ &= -\frac{\overline{z_m}}{\overline{h}} \left(-\Delta x(0) \overline{v_g(-h)' h'} - \int_{x_W}^{x_E} \int_{-h}^{0} v_{BCg} dz dx - AMOC_E \right) \\ &\quad -\frac{\overline{z_m}}{\overline{h}} \left(\int_{x_W}^{x_E} \int_{-h}^{0} v_{BCg} dz dx + AMOC_E \right) + \Delta x(0) \overline{v_g(-h)' min(h, -z_m')} \\ &= \Delta x(0) \left(\frac{z_m}{\overline{h}} \overline{h' v_g(-h)'} + \overline{min(h, -z_m)' v_g(-h)'} \right) \\ &= AMOC_{g-EM} \end{aligned}$$

The contributions of Ekman and baroclinic geostrophic velocities to the external mode are cancelled by that of the barotropic geostrophic velocity due to the no net integral flow constraint. As a consequence, only zonal covariances of the latter with either bathymetry or the upper limb depth are a source of external mode transport, without causing any net integral flow.

SI6: Sensitivity tests

Boundary definition

We have proposed in section SI4 two AMOC reconstructions under variable topography, differing only by the $AMOC_{g-sh}$ transport formulation. The former considers a single western and eastern boundary, and the latter considers multiple western and eastern boundaries. The location and depth of boundaries are displayed in Fig.SI4a-b with a single boundary, and in Fig.SI4c-d with multiple boundaries. In the single boundary case, zonal boundaries are defined at each depth and latitude as the westernmost and easternmost oceanic grid cell. They are mostly located in the steep continental slopes near the coastline. Mid-oceanic ridges and the western flank of the Caribbean archipelago are mostly neglected, as a consequence of the strictly monotonic topography assumption. In the multiple boundary case, western (respectively eastern) boundaries are all oceanic grid cells neighbouring a continental grid cell to the west (respectively to the east). As a consequence, all but flat bottom grid cells are located at a zonal boundary. In particular, both flanks of mid-oceanic ridges and islands are included in this boundary definition. In both cases, the deepest bathymetry h_b is deduced at each latitude from the depth of the deepest boundary grid cell.

Fig.SI5 displays the Hovmoeller diagram of a) the total AMOC reconstruction and b) its geostrophic shear contribution as a function of latitude in the multiple boundary case. Similarly to the single boundary case, the AMOC reconstruction is able to capture the centennial AMOC cycle of CNRM-CM6 both in terms of phase and amplitude. The similarity between both reconstructions shows the dominant role of westernmost and easternmost densities in setting the $AMOC_{g-sh}$ variability. Main differences between both definitions occur in the $10-30°N$ latitude band, suggesting some contribution of the Caribbean islands and Florida peninsula to the $AMOC_{g-sh}$ variability. In the $10-20°N$ latitude band, the AMOC variability is improved and reduced with multiple boundaries, whereas in the $20-30°N$ latitude band, it is noisier and partly out of phase with the total AMOC. This latter result is likely related to errors in the external mode transport reconstruction, as it largely dominates the AMOC at those latitudes (e.g. (McCarthy et al. 2015)). It could be related to the geostrophic assumption of bottom velocities, or numerical errors related to NEMO model's Arakawa-C grid.

Fig.SI6 displays the Talyor diagram of the AMOC reconstruction with a single boundary and multiple boundaries as a function of the total AMOC averaged over latitude bands (colored symbols) and its full meridional average over the $30°S-60°N$ latitude band excluding the Deep Tropics (black symbols). It confirms quantitatively the results found in the Hovmoeller diagram. Under either boundary definition, the AMOC reconstruction explains most of the AMOC variance at all latitude bands. The multiple boundary definition overperforms the single boundary one in terms of correlation at all latitude bands but between $15-30°N$. Overall, the westernmost and easternmost boundary densities explain most of the low-frequency AMOC variability.

Inclusion of the external mode

The bottom currents map (Fig.2c) suggests that the external mode plays a significant role in the total AMOC at western boundaries and in subpolar latitudes. We diagnose here the added value of including it to the AMOC reconstruction. Fig.SI6 evaluates in a Taylor diagram the single boundary AMOC reconstruction with (circles) and without (lower triangle) the external mode contribution. There is no clear added value of including the external mode to the reconstruction of the multidecadal AMOC variability. Indeed, at all latitude bands, the AMOC reconstruction without the external mode explains over 80% of the AMOC variance ($r > 0.9$), with a normalized standard deviation within 30% of unity and a normalized root mean squared error below 0.5. Including the external mode marginally improves the normalized standard deviation and reduces the error of the meridional average, but this results from compensation between latitude bands as the improvement is overall not evident. We conclude that the inclusion of the external mode is physically motivated but it contributes marginally to the AMOC low-frequency variability in CNRM-CM6.

References

Baehr, J., J. Hirschi, J.-O. Beismann, and J. Marotzke, 2004: Monitoring the meridional overturning circulation in the north atlantic: A model-based array design study. *Journal of Marine Research*, **62 (3)**, 283–312, doi:doi:10.1357/0022240041446191, URL https://www.ingentaconnect.com/content/jmr/jmr/2004/00000062/00000003/art00001.

Fox-Kemper, B., R. Ferrari, and R. Hallberg, 2008: Parameterization of mixed layer eddies. part i: Theory and diagnosis. *Journal of Physical Oceanography*, **38 (6)**, 1145–1165, doi:10.1175/2007JPO3792.1, URL https://doi.org/10.1175/2007JPO3792.1, https://doi.org/10.1175/2007JPO3792.1.

Gent, P., and J. McWilliams, 1990: Isopycnal mixing in ocean circulation models. *J. Phys. Oceanogr.*, **20**, 150–155.

Griffies, S. M., and Coauthors, 2016: Omip contribution to cmip6: experimental and diagnostic protocol for the physical component of the ocean model intercomparison project. *Geo-*

scientific Model Development, **9 (9)**, 3231–3296, doi:10.5194/gmd-9-3231-2016, URL https://www.geosci-model-dev.net/9/3231/2016/.

Hirschi, J., and J. Marotzke, 2007: Reconstructing the meridional overturning circulation from boundary densities and the zonal wind stress. *Journal of Physical Oceanography*, **37 (3)**, 743–763, doi:10.1175/JPO3019.1, URL https://doi.org/10.1175/JPO3019.1, https://doi.org/10.1175/JPO3019.1.

Lozier, M. S., and Coauthors, 2019: A sea change in our view of overturning in the subpolar north atlantic. *Science*, **363 (6426)**, 516–521, doi:10.1126/science.aau6592, URL https://science.sciencemag.org/content/363/6426/516, https://science.sciencemag.org/content/363/6426/516.full.pdf.

Lozier, S. M., and Coauthors, 2017: Overturning in the subpolar north atlantic program: A new international ocean observing system. *Bulletin of the American Meteorological Society*, **98 (4)**, 737–752, doi:10.1175/BAMS-D-16-0057.1, URL https://doi.org/10.1175/BAMS-D-16-0057.1, https://doi.org/10.1175/BAMS-D-16-0057.1.

McCarthy, G., and Coauthors, 2015: Measuring the atlantic meridional overturning circulation at 26°n. *Progress in Oceanography*, **130**, 91 – 111, doi:https://doi.org/10.1016/j.pocean.2014.10.006, URL http://www.sciencedirect.com/science/article/pii/S0079661114001694.

Mercier, H., and Coauthors, 2015: Variability of the meridional overturning circulation at the greenland-portugal ovide section from 1993 to 2010. *Progress in Oceanography*, **132**, 250 – 261, doi:https://doi.org/10.1016/j.pocean.2013.11.001, URL http://www.sciencedirect.com/science/article/pii/S0079661113002206, oceanography of the Arctic and North Atlantic Basins.

Voldoire, A., and Coauthors, 2019: Evaluation of cmip6 deck experiments with cnrm-cm6-1. *Journal of Advances in Modeling Earth Systems*, doi:10.1029/2019MS001683, URL https://doi.org/10.1029/2019MS001683.

LIST OF FIGURES

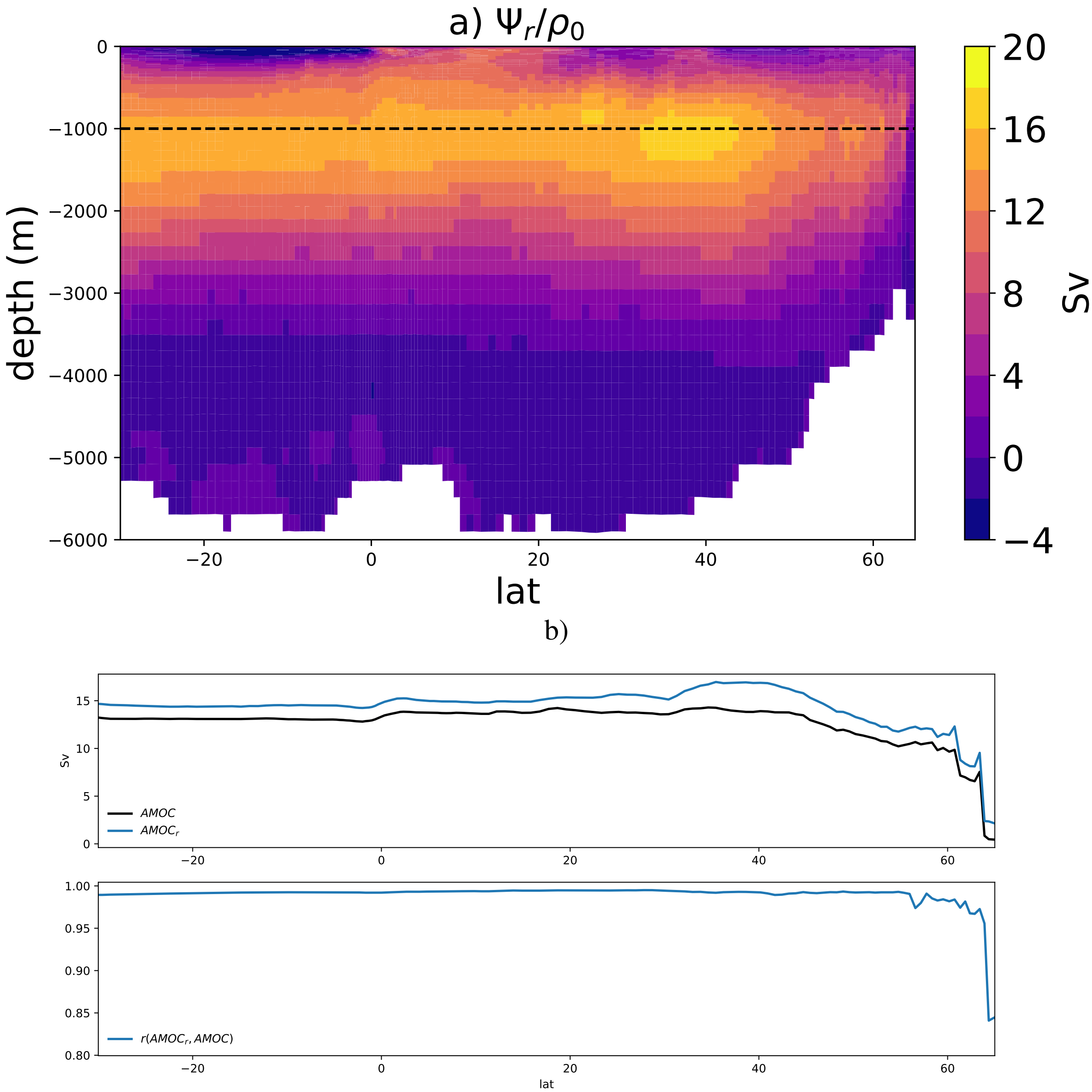

Figure SI 1. a) Average residual Atlantic meridional overturning stream function (Ψ_r/ρ_0 in Sv, with $\rho_0 = 1025kg/m^3$) in CNRM-CM6. Ψ_r represents the residual mean mass transport (in kg/s) that includes the Eulerian mean circulation plus the parametrized eddy-driven mass overturning. The dashed black line shows the depth $z_m = -997m$ of maximum overturning. b) (top) Atlantic Meridional Overturning Circulation deduced as the depth-maximum Eulerian mean ($AMOC$, black) and residual mean ($AMOC_r$, blue) stream function, and (bottom) their interannual correlation ($r(AMOC_r, AMOC)$) in CNRM-CM6.

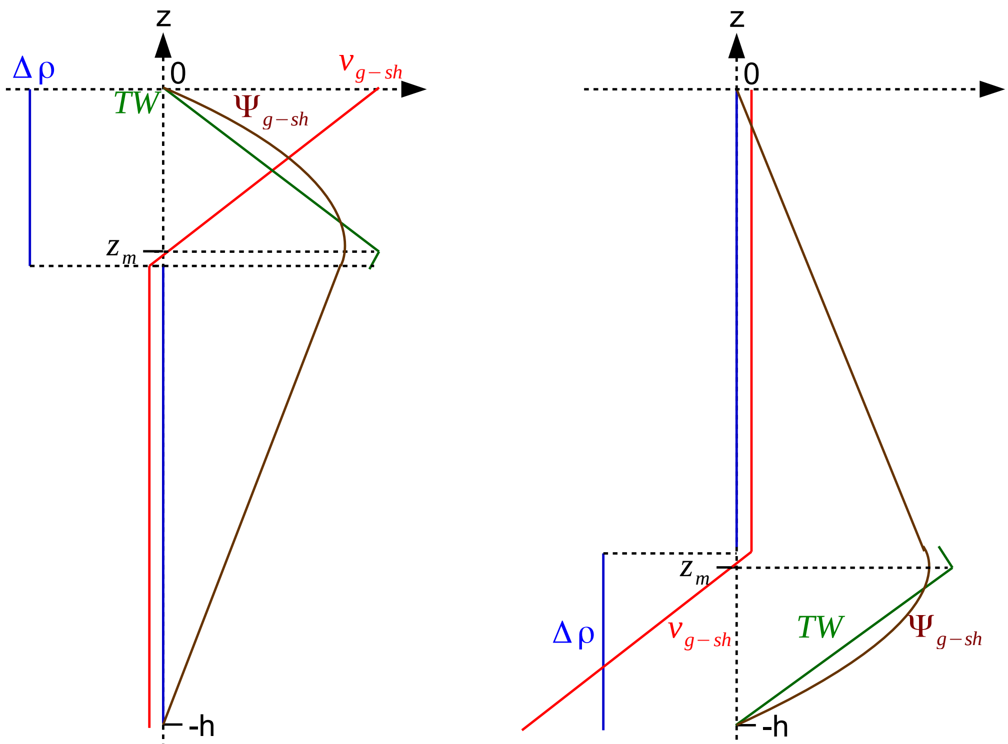

Figure SI 2. Control of the maximum overturning depth z_m by the density anomaly profile $\Delta\rho(z)$. Two vertically-symmetric cases are shown to illustrate how the depth where $\Delta\rho(z)$ (blue) occurs controls the vertical profile of the sheared geostrophic velocities (v_{g-sh}, red), their overturning stream function (Ψ_{g-sh}, brown), the value of z_m and ultimately the thermal wind transport (TW, green). For illustrative purposes, we assume that the overturning is entirely determined by sheared geostrophic velocities v_{g-sh}.

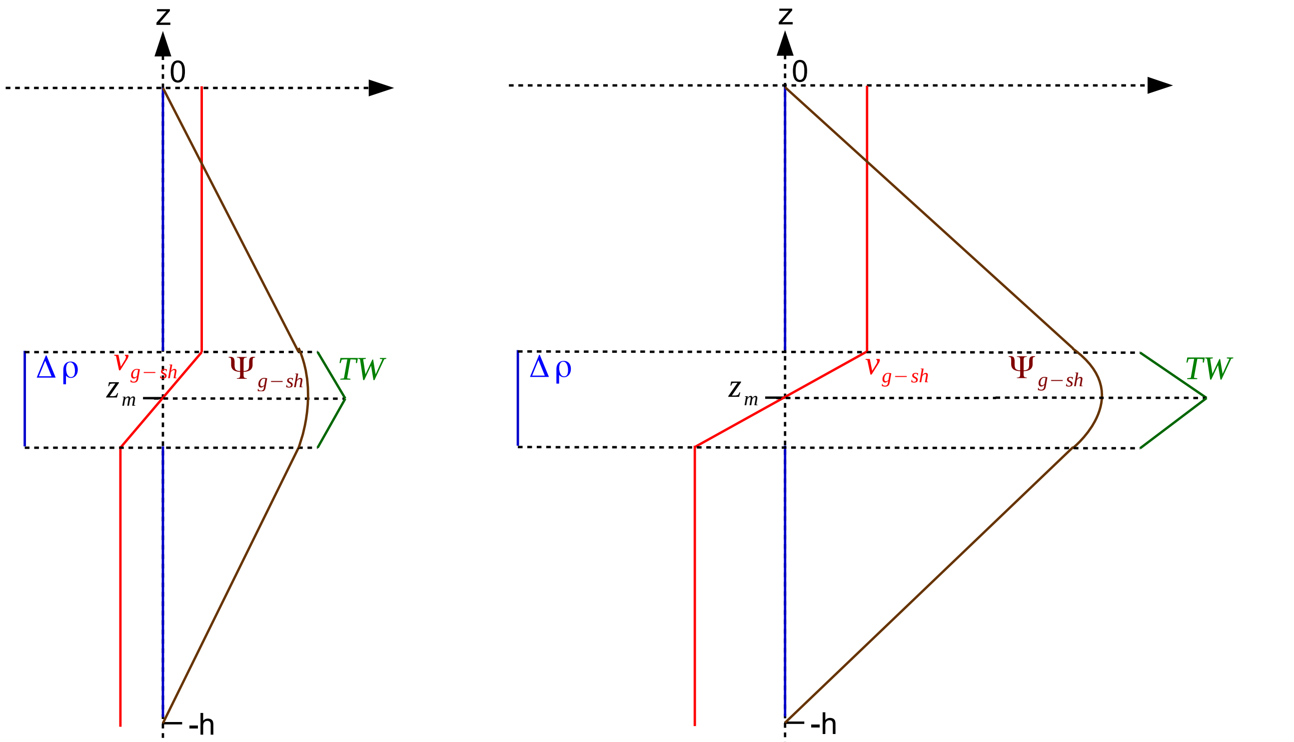

Figure SI 3. Control of the thermal wind transport TW by the magnitude of density anomalies. Two cases are shown to illustrate that for a given maximum overturning depth z_m, the thermal wind transport TW (green) at a given depth is proportional to the magnitude of the density anomaly $\Delta\rho$ (blue). Sheared geostrophic velocities (v_{g-sh}, red) and their overturning stream function (Ψ_{g-sh}, brown) are also shown. For illustrative purposes, we assume that the overturning is entirely determined by sheared geostrophic velocities v_{g-sh}.

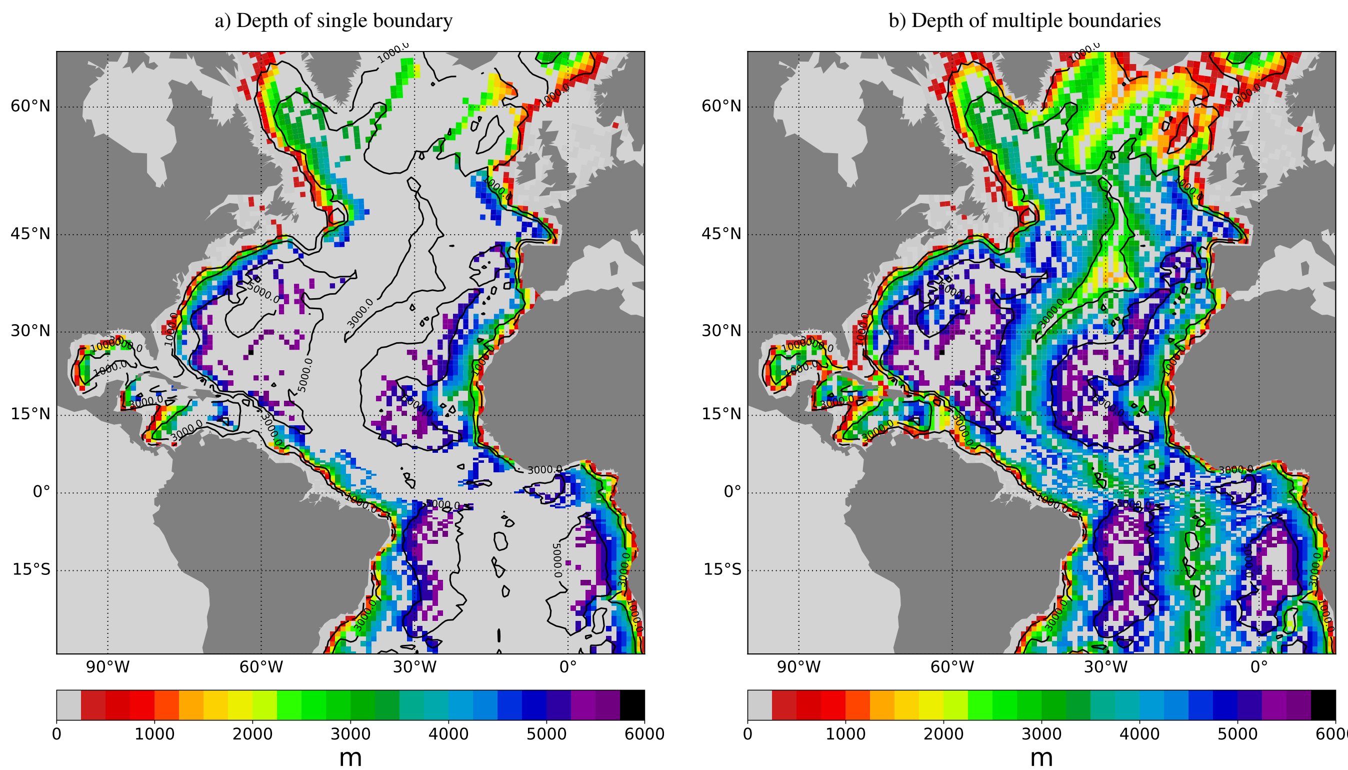

Figure SI 4. Depth of zonal boundaries used for the geostrophic shear transport reconstruction $AMOC_{g-sh}$ (shades) in the a) single and b) multiple boundary case. Bathymetric contours are displayed in black.

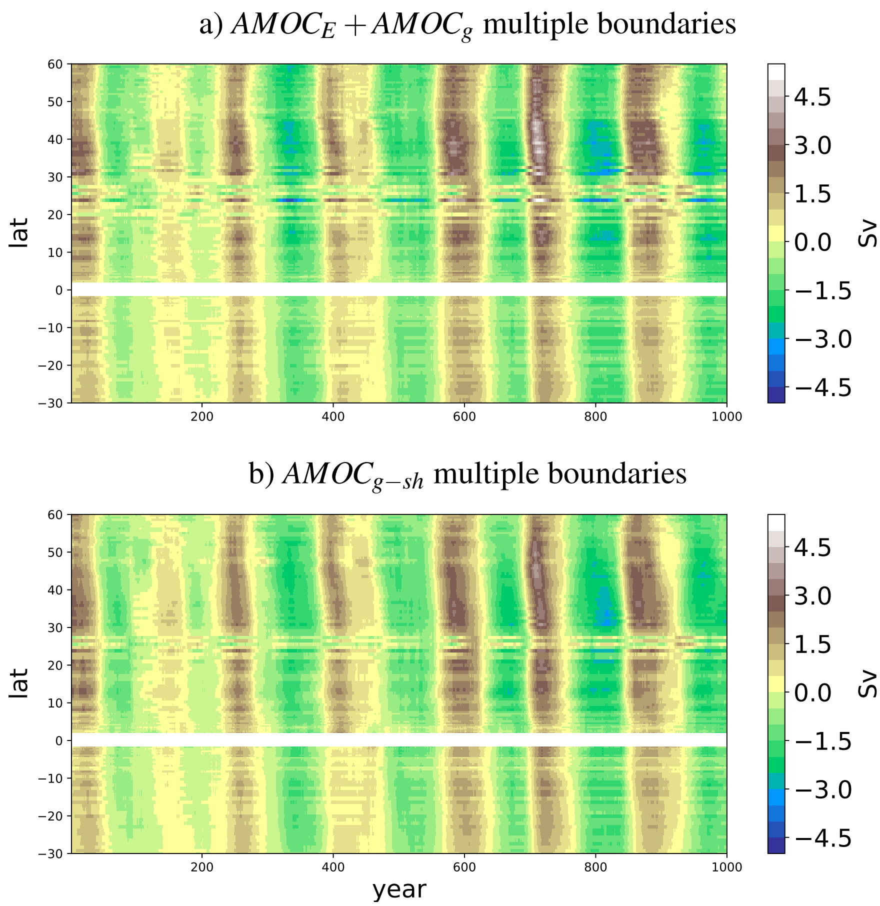

Figure SI 5. Hovmoeller diagram of the 25-year average a) AMOC reconstruction anomaly ($AMOC_E + AMOC_g$) and b) its geostrophic shear component ($AMOC_{g-sh}$) when considering multiple western and eastern boundaries at each latitude and depth.

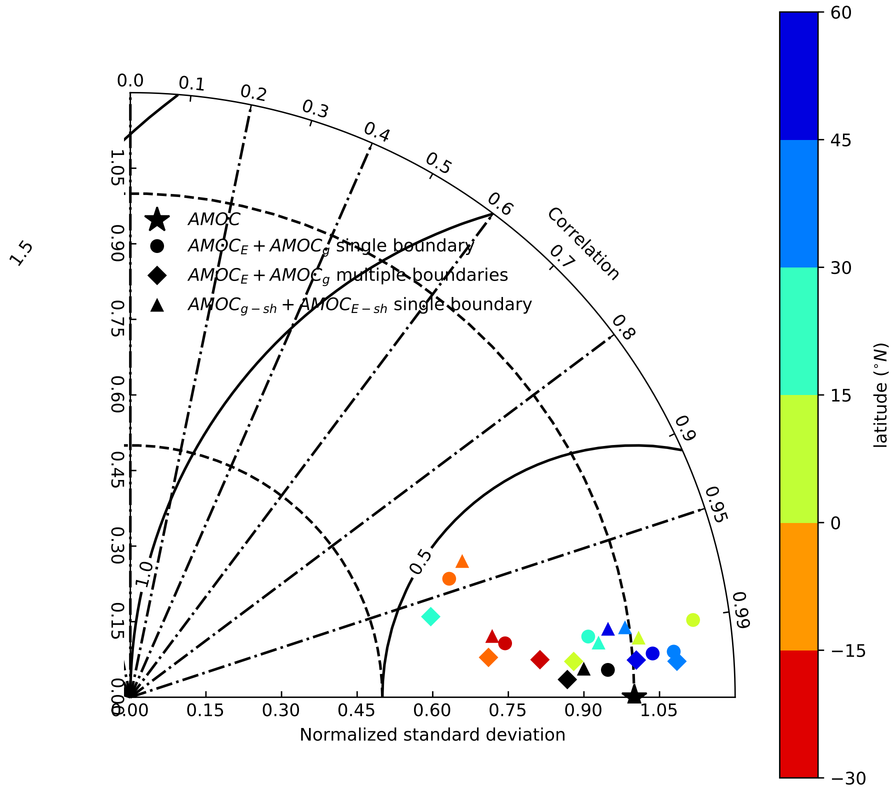

Figure SI 6. a) Taylor diagram of the 25-year average AMOC reconstruction with single boundary (circles), multiple boundaries (diamonds), and with a single boundary when excluding the external mode (lower triangle), as a function of the total AMOC (star). Colors indicate the latitude (15° average), with black symbols the full meridional average over the $30°S-60°N$ latitude band excluding the Deep Tropics (black symbols).